

Observing Sea Surface Current by Gaofen-3 Satellite Along-Track Interferometric SAR Experimental Mode

Xinzhe YUAN^{1,2}, Mingsen LIN^{1,2}, Bing Han^{3,*}, Liangbo ZHAO⁴, Wenyu WANG⁵, Jili SUN³ and Weili Wang⁶

Abstract—Sea surface current is a research hotspot in oceanography. Space-borne along-track interferometric Synthetic Aperture Radar (along-track InSAR, ATI) is a promising sensor for measuring high-resolution sea surface current field, and there is no operational system in orbit yet. To support future space-borne ATI systems, based on the ATI experimental mode of the Gaofen-3 (GF-3) satellite, the first sea surface current observing experiment was conducted in the Jiaozhou Gulf in China in 2019. Meanwhile, SAR observations and in-situ instrument measurements of the current are obtained in the experiments. The data is firstly preprocessed by a processor specially developed for the GF-3 ATI data. Then, the current is extracted based on the M4S mode. The retrieved current of the Jiaozhou Gulf is compared with ground-based High Frequency Surface Wave Radar (HFSWR) data. The results show that the root mean square error (RMSE) of the surface current observed by the GF-3 satellite is less than 0.2 m/s.

Keywords—Sea surface current; Along-Track Interferometric SAR; Gaofen-3 satellite.

I. INTRODUCTION

SEA surface current is one of the most important general movements of ocean water, and it is also a crucial element in ocean observation and marine scientific research. Besides, it may have a major impact on marine climate, marine pollution, fisheries, coastal development, military operations, and so on [1–2].

Among space-borne sensors, Synthetic Aperture Radar (SAR) can obtain high-resolution sea surface parameters. There are two methods for measuring sea surface current by SAR. One is the Doppler centroid analysis (DCA) [3–5] that extracts sea surface current by estimating the Doppler frequency shift of

radar echo caused by current movements. The DCA method is easily applied to conventional SAR. The other one is the along-track interferometric SAR (along-track InSAR, ATI). Comparing with the DCA method, the accuracy of the ATI method is not sensitive to wind speed, and the extracted current field has a higher resolution. In 1987, Goldstein and Zebker from the NASA Jet Propulsion Laboratory [6] first proposed the concept of measuring high-resolution sea surface current by ATI and verified the feasibility of this concept by airborne flight experiments. The fundamental of the ATI method is that the phases of two complex SAR images acquired from the same scene and the same antenna have a short time lag, and the difference of the phases is proportional to the line-of-sight velocity of the targets. Based on this, a plethora of research focused on the methods of inverting current based on ATI data and conceptual ATI systems [7–8]. Meanwhile, a large number of experiments have been performed to demonstrate the effectiveness of the ATI method on different platforms such as aircraft, space shuttle, and satellite [9–18]. The space-borne ATI is the most promising system to extract high-resolution sea surface current owing to its global observation capability during the long lifetime in an orbit. The ATI can be implemented in a satellite in two ways. The one is to split an antenna into two halves to receive radar echo. The ATI system has a short interference baseline when it is applied to a single satellite, such as the dual receive antenna (DRA) mode and the aperture switching (AS) mode of the TerraSAR-X satellite [19], as well as the moving object detection experiment (MODEX) mode of the Radarsat-2 satellite [20]. The other one is satellite formation, and the representative systems are TerraSAR-X and TanDEM-X formations. These two systems form interference baseline through antennas, and they are equipped in different satellites [21–22]. The suitability of these systems is evaluated through theoretical analysis and experimental verification [23]. The evaluation result shows that the satellite formation has advantages in measuring the sea surface current because it has

Funding: This research was funded by National Natural Science Foundation of China “Study on remote sensing mechanisms and low backscattering information extraction of Zhoushan upwelling by space-borne synthetic aperture radar” (Grant No. 41976174) and “China High Resolution Earth Observation System Program” (Grant No. 41-Y30F07-9001-20/22). (Corresponding author: Bing Han.)

¹ National Satellite Ocean Application Service, Beijing 100081, China; harley_yuan@mail.nsoas.org.cn, mslin@mail.nsoas.org.cn

² Key Laboratory of Space Ocean Remote Sensing and Application, Ministry of Natural Resource of the People’s Republic of China, Beijing 100081, China;

³ Aerospace Information Research Institute, Chinese Academy of Sciences; Beijing 100094, China; han_bingl@mail.ie.ac.cn; sunjl@aircas.ac.cn ;

⁴ Institute of Remote Sensing Satellite, China Aerospace Science and Technology Corporation, Beijing 100094, China; 13718896255@139.com;

⁵ Key Laboratory of Microwave Remote Sensing, National Space Science Center, Chinese Academy of Sciences, Beijing 100190, China; wangwenyu@mirslab.cn;

⁶ North China Sea Marine Forecasting Center, Ministry of Natural Resources, Qingdao 266061, China; wangweilice@hotmail.com;

Received: date; Accepted: date; Published: date

a long baseline that is close to the theoretical analysis. The ATI system with a short baseline achieves the same performance as DCA. Besides, some conceptual ATI systems such as dual-beam interferometry (DBI) were also proposed to measure the two-dimensional current fields [24].

Besides the above-mentioned experimental systems, there is no operational civilian satellite supporting the ATI technique. To provide the ATI technique for future satellites and verify its effectiveness, for the first time, the current measurement experiments based on ATI are conducted on China's Gaofen-3 satellite (GF-3) [25] from 2018 to 2019. The details of the experiments are introduced in the paper. The rest of this paper is organized as follows. Section 2 introduces the acquired experiment data. Section 3 describes the characteristics of the experiment datasets, including GF-3 satellite ATI mode data, ground-based High Frequency Surface Wave Radar (HFSWR) data, and wind field data. The data preprocessing method specially developed for the GF-3 data and wind field data is present in Section 4. The current extraction method adopted in this work is introduced in Section 5. The accuracy of the inversed current field is evaluated by comparing it with the HFSWR data in Section 6. Section 7 gives the conclusions and discusses the further research work.

II. DATA ACQUISITION

The sea current measurement experiments on the GF-3 satellite were organized by National Satellite Ocean Application Service (NSOAS). The experiments were conducted in the Beibu Gulf and Jiaozhou Gulf from 2018 to 2019. The radar parameters are specially set by the Institute of Remote Sensing Satellite (IRSS, CAST) because the ATI mode is an experimental mode of the GF-3 satellite. The radar echo imaging process is completed by the Aerospace Information Research Institute (AIRI, CAS) based on a modified GF-3 data processor. The HFSWR data of the Jiaozhou Gulf and the sea current meters data are provided by the Beibu Gulf North China Sea Marine Forecasting Center, Ministry of Natural Resources (NCSFC, MNR), Beihai Marine Environment Monitoring Center Station, and Ministry of Natural Resources (BHEMNC, MNR). From April 8 to April 27, 2018, five satellite observations were conducted in the Beibu Gulf, Guangxi Zhuang Autonomous Region, China. About fifty SAR image pairs were acquired in the experiment. Unfortunately, since there are anomalies in the sea current meters data of the satellite observing area, only the function of the ATI mode was validated in the experiment.

To further verify the effectiveness of the current measurement based on ATI, other experiments were conducted on October 29, 2019, in the Jiaozhou Gulf, Shandong Province, China. Five image pairs were obtained in the experiment. The specific observing time and areas are listed in Table I.

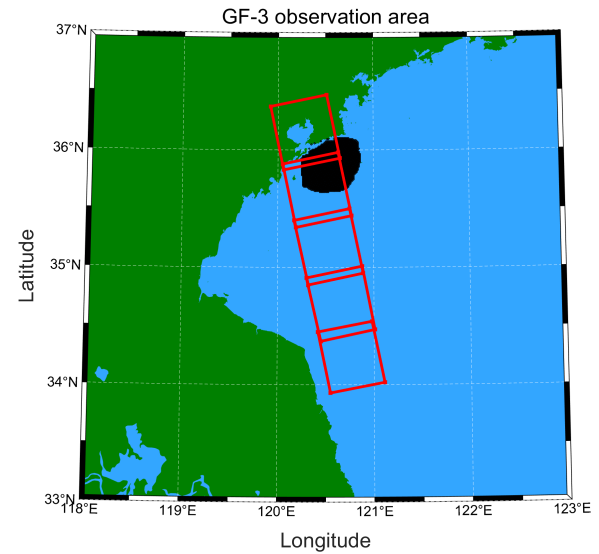


Fig. 1. GF-3 satellite observation area (red) and HFSWR measurement area (black) in the Jiaozhou Gulf experiment in 2019

TABLE I
GF-3 SATELLITE DATA ACQUIRED IN THE JIAOZHOU GULF

Index	Observing time (UTC)	Observing area	Direction	Antenna look direction
a	2019-10-29 09:49:34	120.78°E, 34.24°N	Ascent	Right
b	2019-10-29 09:49:42	120.67°E, 34.69°N	Ascent	Right
c	2019-10-29 09:49:50	120.55°E, 35.18°N	Ascent	Right
d	2019-10-29 09:49:58	120.42°E, 35.66°N	Ascent	Right
e	2019-10-29 09:50:06	120.30°E, 36.15°N	Ascent	Right

In this experiment, a part of the observing area is also measured by the HFSWR located on Xueja Island. The schematic diagram of the area observed by the partial voyage satellite is illustrated in Fig. 1 (the red rectangles in the figure represent the satellite observation areas, and the black marks represent the measurement positions of the HFSWR during satellite observations).

III. EXPERIMENT DATA SET

A. GF-3 satellite ATI experimental mode

The GF-3 satellite is the first civil C-band polarimetric SAR in China. Its highest resolution is 1 m, and its largest swath reaches 650 km. Besides 12 formal imaging modes, the satellite also supports the ATI experimental mode to observe the moving target.

For the ATI mode, the antenna with a length of 15 meters is divided into two sub-apertures with an identical length, forming two interferometric channels in the azimuth. The principle of the ATI mode of the GF-3 satellite is similar to that of the DRA mode of the TerraSAR-X satellite [26], that is, the full aperture sends a signal, and the two sub-apertures simultaneously

receive the echo. As shown in Fig. 2, the center of the full aperture phase is at a_0 , and the centers of the two sub-apertures receiving phases are respectively at a_1 and a_2 . The range between a_1 and a_2 is $2B$. The phase center of the echo signals received by sub-aperture 1 is at the center of the line connecting a_1 and a_0 , while that of the echo signals received by sub-aperture 2 is at the center of the line connecting a_2 and a_0 . The signals received by apertures 1 and 2 can form an interferometric baseline in azimuth with the length of $B = 3.75\text{m}$. The radar parameters of the ATI mode of the GF-3 satellite are listed in Table II.

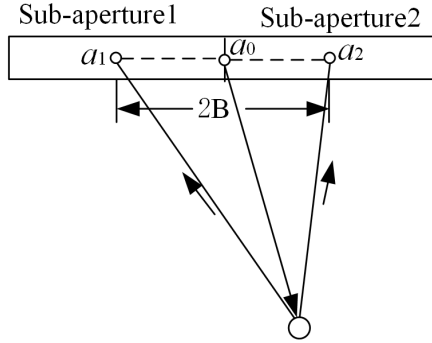


Fig. 2. Schematic diagram of the SAR-ATI mode of the GF-3 satellite

TABLE II
THE RADAR PARAMETERS OF THE GF-3 ATI EXPERIMENTAL MODE

Radar parameter	Values
Transmitting signal center frequency	5.4 GHz
Platform altitude	755 km
Satellite speed	7500 m/s
Antenna length	15 m
ATI mode	Full aperture transmission, dual aperture reception
Effective ATI baseline length	3.75 m
Transmit signal bandwidth	50MHz
Polarization mode	VV, HH
Incident angle	15-50°
Pulse repetition frequency	2202-2606 Hz
NESZ	-20 dB

The interferometric phase of the ATI mode can be expressed as follows [27]:

$$\Delta\phi = \frac{4\pi v_r B}{\lambda v_s}, \quad (1)$$

where $\Delta\phi$ is the along-track interferometric phase; λ is the radar wavelength; B is the effective along-track baseline; v_s is the platform speed, and v_r is the ocean surface line of sight (LOS) velocity. According to the system parameters listed in Table II, when the interferometric phase is in the range of $(-\pi, \pi]$, the unambiguous ocean surface speed that can be measured ranges from -28.57 m/s to $+28.57\text{ m/s}$. Therefore, phase unwrapping can be ignored.

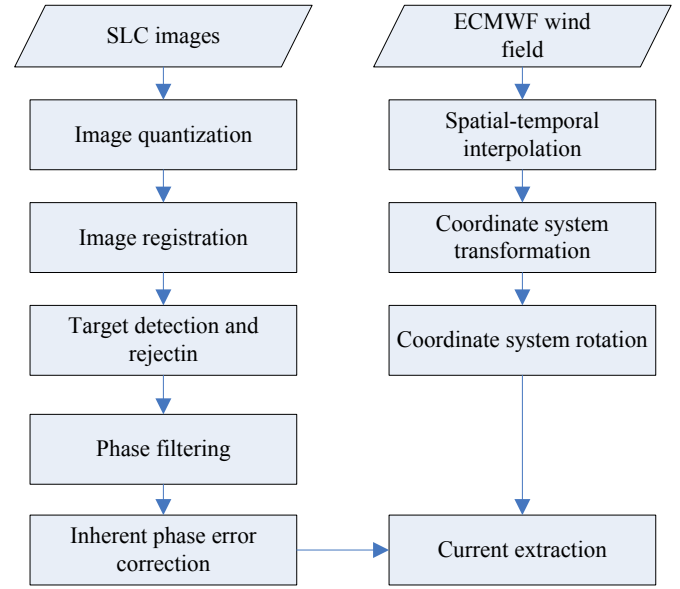


Fig. 3. Data preprocessing flow

B. Characteristic of images

The radar echo is processed by the GF-3 satellite data processor, and the Chirp Scaling algorithm [28] is adopted to generate Single Look Complex (SLC) image pairs. Since ATI mode is not a formal imaging mode, the processing parameters are modified. The specifications of the ATI mode for SLC images are listed in Table III.

TABLE III
SPECIFICATION OF SLC IMAGES

Image parameters	Values
Quantization digit	16 bit
Image size	Azimuth 20000 pixel Range 24000 pixel
Nominal spatial resolution	Azimuth 5 m Range 5 m
Image size	Azimuth 50 km Range 60 km

C. HFSWR data

A type of “COADS Seasonde” HFSWR simultaneously measures the current in the Jiaozhou Gulf. The nominal parameters of it are listed in Table IV.

TABLE IV
THE PARAMETERS OF THE HFSWR

System parameter	Values
Radar frequency	24.5MHz
Type	COADS Seasonde
Range resolution	500m-3km
Angular resolution	1-5°
Nominal Radial velocity accuracy	<7 cm/s

The HFSWR data is recorded on 10:00 (UTC), October 29, 2019, within the region from 120.25°E, 35.64°N to 120.86°E, 36.10°N. The actual resolution is 1 km and the angular

resolution is 5° . The root-mean-square error (RMSE) of the radial velocity accuracy is less than 8 cm/s, which was assessed by NCSFC in 2019 through a comparison with the seabed-based ADCP data.

D. Input wind field

Sea surface wind field data of the satellite observation area is necessary when the current is extracted. The European Centre for Medium Weather Forecasts (ECMWF) reanalysis wind field (ERA3) is used in the experiment because there is no on-site wind measurement instrument in the experiments. Its time resolution is 6 hours and spatial resolution is 0.25° (about 25 km).

IV. DATA PREPROCESSING

Two kinds of data need to be processed before current extraction. The one is the SLC image pairs that are generated by the GF-3 data processor, and the other is the ECMWF wind field. The interferometric phase images and the wind field generated in preprocessing are used as input for the M4S mode.

The preprocessing steps are demonstrated in Fig. 3, and the details are described in the following sections.

A. Image quantization

Based on the two-channel data quantized values provided in the auxiliary documentation of the GF-3 product, the SLC images are quantized according to equation (2).

$$s = DN_i/32767 \cdot QV + j \cdot DN_q/32767 \cdot QV, \quad (2)$$

where s is the single-channel data; DN_i and DN_q indicate channel I and Q, respectively; QV is the quantized data of the channel, and j is the imaginary unit.

B. Image registration

Fig. 2 shows that the azimuth distance between the equivalent phase centers of the front and rear apertures is Δd . The rear aperture data is transformed into the Doppler domain where a linear phase is multiplied. After that, an inverse Fourier transform is performed to convert the data to the time domain. The transformation is shown in equation (3).

$$s_{ar} = IFFT \left(FFT(s_a) \cdot \exp \left(-j \cdot 2\pi \cdot f_d \cdot \frac{\Delta d}{v_s} \right) \right), \quad (3)$$

where s_a is the rear aperture data that is to be registered; j is the imaginary unit; f_d is the Doppler frequency; Δd is the azimuth distance between the two channels; v_s is the satellite velocity; FFT means the Fast Fourier Transformation, and $IFFT$ means the Inverse Fast Fourier Transformation.

C. Target detection and rejection

Strong scattering targets are common in SAR images such as ships, buoys, and so on. These moving targets can cause additional phases, while the stationary targets have a zero phase in theory. As for the two kinds of targets, their phase is different

from the sea surface, which needs to be rejected before subsequent processing.

The two-parameter constant false-alarm rate algorithm (2P-CFAR) is exploited to detect the targets [29]. Since the algorithm is essentially a sliding window method, it takes a long time in data processing [30]. In practice, an empirical threshold T that is equal to $5 \sim 5.5$ is adopted. Based on the detection results, the phase of the targets in the phase image is set to the mean phase.

D. Phase filtering

Since the current velocity is low, the corresponding interferometric phase is also small. Thus, the neighborhood

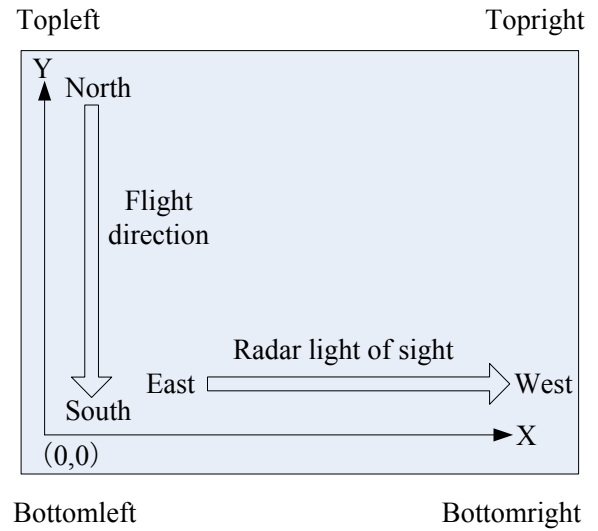


Fig. 4. Geometry relationship between the GF-3 satellite SLC image and the geography coordinate system in the condition of radar right side look on an ascending orbit

averaging operation needs to be performed to improve the signal-to-noise ratios and phase sensitivities. In our work, the phase image with a resolution of 300×300 pixels is processed by neighborhood averaging, that is, the spatial resolution of the processed phase image is close to 1 km. For the noisy phase image, the circular period filtering with a filtering window of 5×5 can be performed several times.

E. Inherent phase error correction

Due to the dual-channel imaging mechanism of the ATI mode, inherent phase errors inevitably appear. Many factors are related to the inherent phase error, such as the inherent error of the radar electronic system, satellite attitude error, antenna

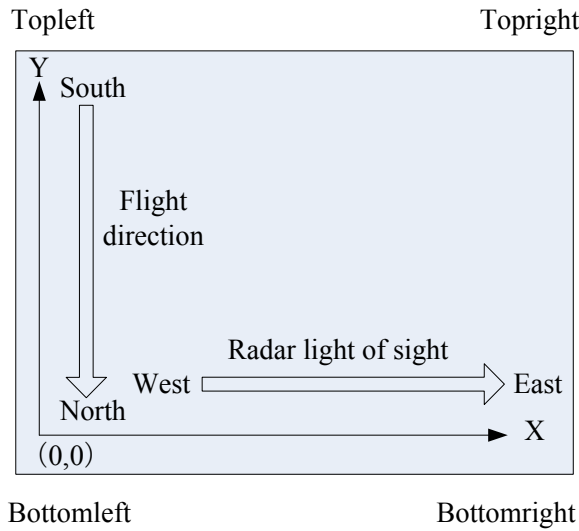


Fig. 5. Geometry relationship between the GF-3 satellite SLC image and the geography coordinate system in condition of radar left side look on a descending orbit

phase center position error, and antenna pattern inconsistency. These errors need to be eliminated before the current extraction [31].

In theory, the interferometric phase in the stationary terrestrial scene is zero. It is feasible to estimate the inherent phase error from the terrestrial scene in the coastal region. In the experiments, it is already designed that the terrestrial scenes are imaged in each satellite observation. Meanwhile, every 300 pixels of the phase images are averaged along the range to estimate the phase errors. For the convenience of current extraction, the number of averaged pixels is consistent with that of the neighborhood averaging processing. The estimated inherent phase error should be eliminated from the other phase images in the same observation.

F. Wind field preprocessing

1) Spatio-temporal interpolation

After data preprocessing, the spatial resolution of the phase image is about 1 km, while that of the ECMWF wind field is about 25 km. The time resolution of the ECMWF wind field is 6 hours. Through Spatio-temporal interpolation operation, the phase images are transformed into wind field data with a resolution of 1 km and satellite observation time of 0.5 hours.

2) Wind field vector coordinate transformation and rotation

The ECMWF wind field data adopts a geography coordinate system. The wind vectors u and v are in the eastward and northward direction, respectively. By contrast, the phase images used in the current extraction adopt an image coordinate system. Unlike some satellites such as the Radarsat-2 satellite, SLC images of GF-3 satellite are processed based on radar echo recording sequences. Different satellite orbits (ascending/descending) and the radar line of sight (left/right side look) cause the radar echo to be recorded in different

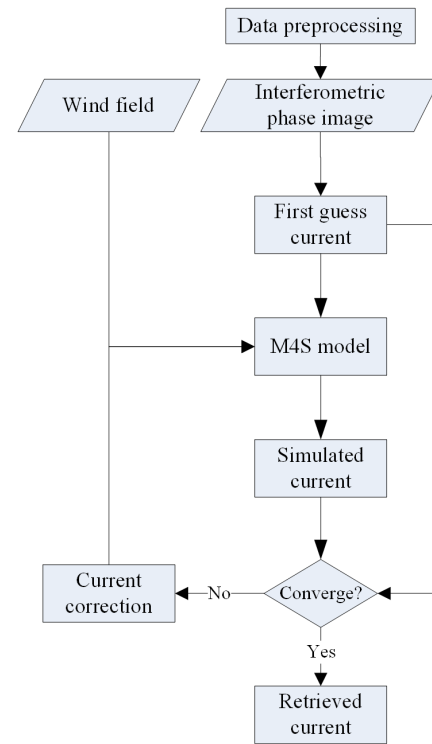


Fig. 6. Process of the current extraction

sequences. Therefore, according to the orbit and radar line of sight, the coordinate system of the GF-3 satellite and the geography coordinate system have different geometry relationships. It is necessary to transform the coordinate system of the ECMWF wind field before current extraction.

Fig. 4 shows the geometry relationship between the GF-3 satellite SLC image coordinate system and the geographic coordinate system in the condition of radar right side look on an ascending orbit. The black arrows X and Y indicate the coordinate axes of the image coordinate system, and the coordinate origin $(0, 0)$ is in the lower-left corner of the image. The hollow arrow parallel to the X -axis represents the radar line of sight direction, and that parallel to the Y -axis represents the radar satellite flight direction in the geographic coordinate system. The geometry relationship in the condition of radar left side look on a descending orbit is shown in Fig. 5.

Besides, the orbit inclination of the GF-3 satellite is about 98 degrees. That is, there is an angle of 8° between the geographic coordinate system and the image coordinate system. Thus, it is also necessary to conduct a coordinate system rotation on the ECMWF wind vectors. The rotation can be described as follows:

$$wind_x = wind_u \cdot \cos(\theta) + wind_v \cdot \sin(\theta), \quad (4)$$

$$wind_y = wind_v \cdot \cos(\theta) - wind_u \cdot \sin(\theta), \quad (5)$$

where $wind_u$ and $wind_v$ represent the ECMWF wind vectors; $wind_x$ and $wind_y$ are the wind vectors in the image coordinate system after coordinate rotation; θ is a positive

angle of 8° in the condition of an ascending orbit, while it is an angle of 8° in the condition of a descending orbit.

V. SEA SURFACE CURRENT INVERSION

An iterative sea surface current inversion method based on the M4S model [32] is exploited to extract current. The M4S developed by Roland Romeiser at Hamburger university is a numerical simulation tool for the microwave radar imaging of the ocean. M4S mode has been widely used in radar signal simulation of sea surface features, such as sea surface current, wind field, and so on. In this work, the measured ATI phase and iterative phase will be compared with the M4S simulation results. The inversion procedure is shown in Fig. 6.

A. Inversion parameters

The radar parameters that are needed by the current inversion include radar frequency, polarization, incident angle, platform velocity, platform altitude, platform heading, radar look direction, spatial resolution, and effective along-track baseline length. These details of these parameters are listed in Table III.

The RMSE between the simulated current field and the first guess current field is used as a threshold to determine whether the retrieval processing is continued. In our work, the threshold is set to 0.05 m/s.

B. First guess current

The horizontal component of the radar line-of-sight velocity is calculated according to equation (6). This velocity refers to the Doppler velocity caused by the sea surface movement such as current, waves, etc. It can be regarded as the initial current used in the iterative retrieval.

$$v_0 = \frac{v_r}{\sin \theta} = -\frac{\lambda V_s \Delta \phi}{4\pi B \sin \theta}, \quad (6)$$

where v_0 is the horizontal component of the radar line-of-sight velocity; v_r is the velocity of the moving target in the radar line of sight; θ is the incident angle; $\Delta \phi$ is the corrected phase; λ is the radar wavelength; V_s is the platform velocity, and B is the effective along-track baseline length.

C. Simulated current field

Based on the M4S model, the simulated along-track interferometric phase and the corresponding simulated current is calculated based on the input of the first guess current and input wind vector.

D. Iterative convergence judgment

The simulated current is compared with the first guess

current. If the RMSE between them is less than the threshold, it is considered that the algorithm converges, and the simulated current in this step is an inverted current field; otherwise, the iterative processing continues.

E. Current correction

The current obtained in step 4 is corrected according to the difference between the M4S stimulation current and the first guess current. The correction is shown as:

$$v_{ij}^n = v_{ij}^{n-1} + \beta \Delta v, \quad (7)$$

where β is the step factor (typically 0.5~1), and Δv is the velocity difference between the simulated current and the first guess current. In our work, an adaptive step factor is used to accelerate convergence.

The corrected current is taken as the input of the M4S model for the next iterative correction until it converges.

VI. RESULTS AND DISCUSSION

Fig. 7 shows the five amplitude images obtained by the experiment in the Jiaozhou Gulf corresponding to the chronological order listed in Table I. Fig. 8(a)~(d) illustrates the scenes in the Yellow Sea, where ships and their wakes are clear. Fig. 8(e) illustrates the terrestrial scene nearby Qingdao city. As discussed in section 4.5, the terrestrial region in this scene was used to estimate the inherent phase errors.

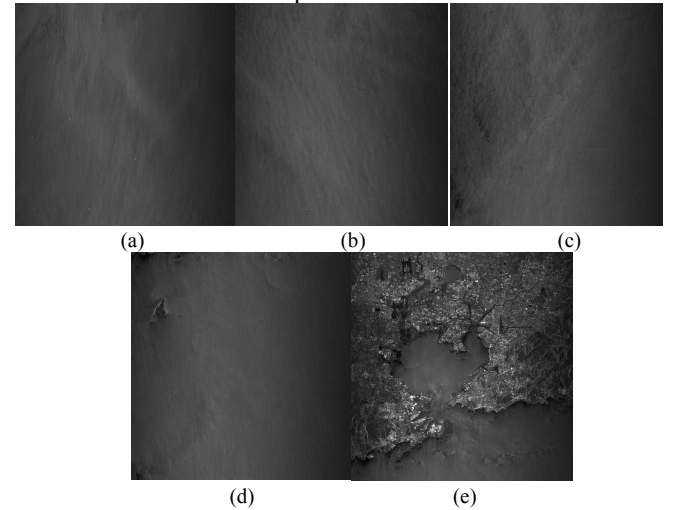


Fig. 7. Amplitude images of the five GF-3 ATI images acquired in the Jiaozhou Gulf. (a)120.78°E, 34.24°N; (b)120.67°E, 34.69°N; (c)120.55°E, 35.18°N; (d)120.42°E, 35.66°N; (e)120.30°E, 36.15°N.

A. Result of data preprocessing

The details of the data preprocessing are listed in Table V.

TABLE V
THE RETRIEVAL RELEVANT PARAMETERS

Scene	a	b	c	d
Pre-Registration coefficient	0.7700	0.7697	0.7696	0.7697
Post-Registration coefficient	0.9916	0.9912	0.9910	0.9910
Detected ship target amount	1411 pixels	526 pixels	411 pixels	206 pixels
Wind u(eastward)	1.91 m/s	2.66 m/s	2.62 m/s	1.41 m/s
Wind v(northward)	-4.53 m/s	-3.73 m/s	-3.82 m/s	-4.67 m/s
Wind x(range)	1.22 m/s	2.09 m/s	2.03 m/s	0.72 m/s
Wind y(azimuth)	-4.76 m/s	-4.08 m/s	-4.16 m/s	-4.82 m/s

The coherence coefficient of the SLC image pairs is 0.7-0.8, and it increases to 0.92-0.97 after the rear aperture data is registered. The wind u and v are the ECMWF wind vectors, while the wind x and y are the wind vectors in the image coordinate system.

The interferometric phase images of the five SLC image pairs after neighborhood averaging and twice circular period filtering are shown in Fig. 8.

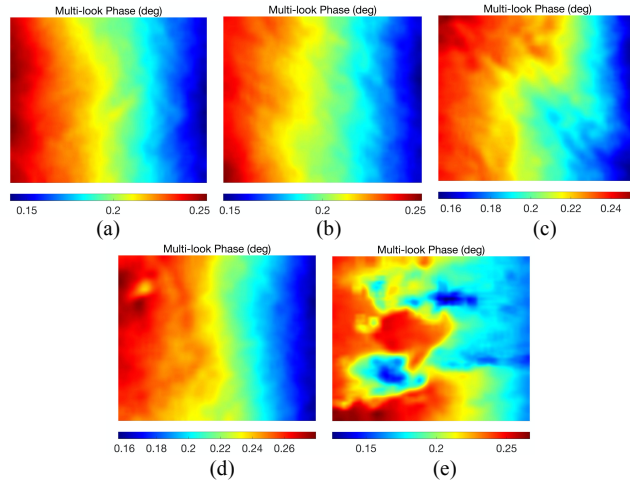


Fig. 8. Filtered phase images of scenes in Fig. 7 (Interpolated to 1000 pixel \times 1000 pixel): (a)120.78°E, 34.24°N; (b)120.67°E, 34.69°N; (c)120.55°E, 35.18°N; (d)120.42°E, 35.66°N; (e)120.30°E, 36.15°N

The inherent phase error estimated from Fig. 7(e) is 0.16-0.24 m/s, which corresponds to a horizontal velocity of -3.67~-5.51 m/s. After the inherent phase error is removed, the horizontal Doppler velocities of the sea surface are obtained from the phase images, and the first guess current corresponding to the scenes in Fig. 7 is shown in Fig. 9.

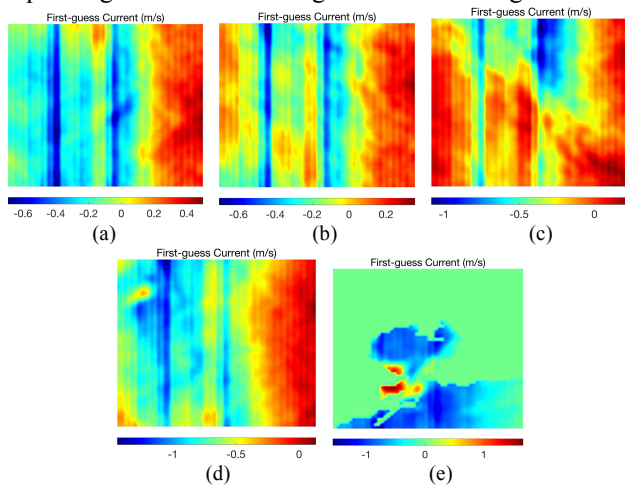


Fig. 9. First guess currents of the scenes in Fig. 7. They were used for the initial field of iteration: (a)120.78°E, 34.24°N; (b)120.67°E, 34.69°N; (c)120.55°E, 35.18°N; (d)120.42°E, 35.66°N; (e)120.30°E, 36.15°N.

B. Result of inversed sea surface current

The algorithm converges after 4~5 iterations. The retrieval currents of the scenes in Fig. 7 are shown in Fig. 10.

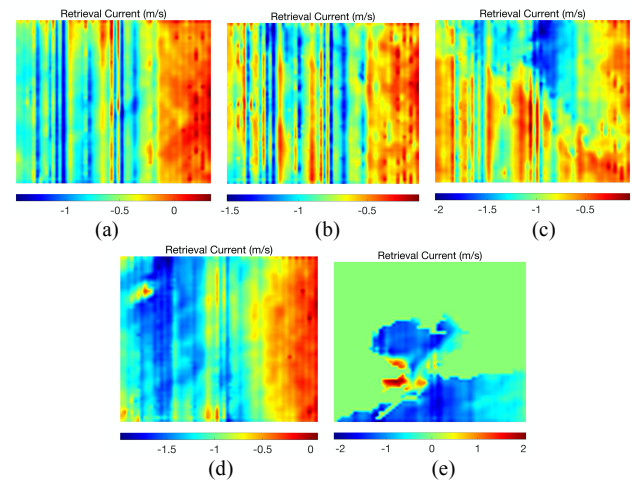


Fig. 10. Retrieval line of the sight currents of the five considered scenes when the iteration converges: (a)120.78°E, 34.24°N; (b)120.67°E, 34.69°N; (c)120.55°E, 35.18°N; (d)120.42°E, 35.66°N; (e)120.30°E, 36.15°N.

C. Accuracy analysis

The retrieval currents of Fig. 7(d) and Fig. 7(e) are evaluated, and the evaluation results are compared with the HFSWR data in the common spatial region that is covered by the SAR and HFSWR shown in Fig. 1.

TABLE VI
MEASURED CURRENTS COMPARISON OF GF-3 AND HFSWR.

Result	Image(d)	Image(e)
Regression Coefficient	1.0359	1.1123
Correlation Coefficient	0.7058	0.5482
Mean Difference	-0.0237	-0.0797
RMSE	0.1998	0.1973

The HFSWR data are collected every 20 minutes by two SeaSonde radars that are manufactured by CODAR Ltd. These two radars are compact high-frequency systems. The ocean surface currents monitored by the HFSWR at two specific moments on Oct 29 in 2019 are shown in Fig. 11, and the currents are general southwest flows. These radar data were examined by ADCP measurements in a field experiment in 2017.

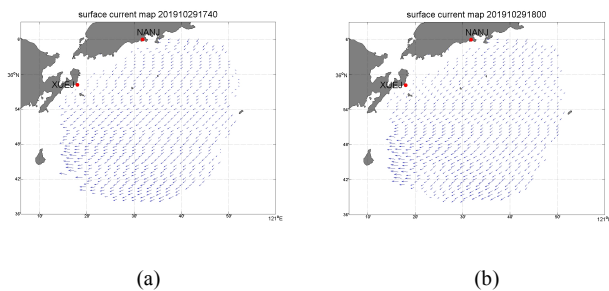


Fig.11. Sea surface currents mapped by HFSWR at (a) 2019/10/29 17:40 and (b) 2019/10/29 18:00. The two radar stations are indicated by red points.

The evaluation results of the currents retrieved from the images (d) and (e) are shown in Fig. 7. The detailed statistics of the comparison are listed in Table VI.

The regression coefficients are 1.0359 and 1.1123 respectively, indicating that the inversed current has a good linear relationship with the HFSWR data. The correlation coefficients between the inversed current and the HFSWR data are 0.7058 and 0.5482, showing good overall consistency. The mean differences between the currents derived from the GF-3 and HFSWR are respectively -0.0237 m/s and -0.0797 m/s, while the RMSE is 0.1998 m/s and 0.1973 m/s, respectively.

Fig. 12 presents the scatter diagrams of the inversed current versus the HFSWR data for the overlap region measured by SAR and HFSWR. Since the inversed currents were averaged to grid cells of about 1 km that are similar to the grid cells of the HFSWR currents, there were no statistical asymmetries caused by different spatial resolutions of the two sensors. The results in the scatter diagrams are consistent with the statistical quantities (listed in Table VI).

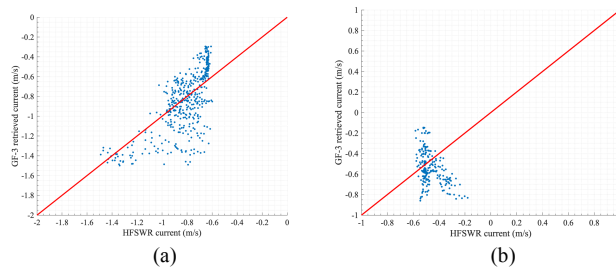


Fig. 12. Scatter diagrams of the GF-3 ATI currents versus the HFSWR currents for the two scenes: (a) scene d; (b) scene e.

VII. CONCLUSIONS

For the first time, based on the ATI mode of the GF-3 satellite, sea surface current observing experiments was performed in the Jiaozhou Gulf in China in October 2019. The one-dimension sea surface current field is extracted from the satellite data. Meanwhile, the accuracy of the inversed sea surface current obtained on October 29, 2019, in the Jiaozhou Gulf is evaluated by comparing the result with the HFSWR data. The statistical quantities of the two currents show relatively good consistency. Also, the RMSE of the two currents is less than 0.2 m/s, and the correlation coefficients are larger than 0.5. Unlike the TerraSAR-X/TanDEM satellite formation where the baseline is formed from different platforms, the GF-3 ATI mode is a short baseline system. Though it is not specially designed to measure sea surface current, its accuracy meets our expectations.

However, some problems need to be addressed in future work. The input wind field is essential for improving the accuracy of inverting sea surface current. Because there are no in situ wind-measuring instruments in the experiments, the ECMWF wind field is used as an alternative. Though the Spatio-temporal interpolation operation is performed on the

ECMWF wind field, there are still some deficiencies in this work. Specifically, the spatial resolution of the ECMWF wind field is coarser than that of the inversed current. Also, the time resolution of the ECMWF wind field is 6 hours, while that of the SAR imaging sea surface is within several seconds. Besides, the input wind field can be extracted from the SAR data itself based on the CMOD geophysical model function, indicating no shortage of ECMWF wind field. Especially, the input wind field can be obtained without a wind-measuring instrument, which is suitable for a future spaceborne ATI system. Unfortunately, the SAR data is not radiometrically calibrated in our experiment because the SAR-ATI of the GF-3 satellite is an experimental mode. The current extraction based on the input wind fields inversed from the SAR data will be studied in follow-up work.

Besides, wind speed is related to the accuracy of the inversed current field by affecting the SNR (Signal-noise ratio) and coherence of phase images. High SNR and coherence are conducive to inverse current. Usually, as wind speed increases, the SNR of the phase image increases but the coherence of the phase image decreases. In this experiment, the wind speed ranges from 3.5 m/s to 5.5 m/s, that is, the experiment is conducted under the condition of low wind speed. Therefore, the analysis of accuracy under different wind speed conditions needs to be further evaluated.

The inherent phase error also has an important influence on the accuracy of current extraction. Many factors are affected by the phase error, such as radar electronic system, platform attitude error, antenna phase center position error, and antenna pattern inconsistency. The error of the radar electronic system is corrected by the internal calibration data in imaging processing. As for the satellite attitude error and the antenna phase center position error, it is equivalent to generate an additional cross-orbit baseline during the imaging process, which causes the phase changes along the range direction. The attitude measurement data of today's satellite is not accurate enough to directly correct the phase errors. In the coastal region, the phase error can be estimated from the images in terrestrial scenes. However, the platform attitude of a satellite in orbit is changing because the yaw steering technique is widely adopted in today's SAR satellite. Therefore, the estimated phase error can be invalid in open-sea current extraction. The correction of the inherent phase error based on the terrestrial scenes is still challenging. The combination of baseline precise measurement and SAR signal processing technique could be a feasible approach, and it needs to be further studied.

REFERENCES

- [1] P. R. Pinet, "Invitation to Oceanography," 8rd ed.; Jones & Bartlett Learning: Massachusetts, USA, 2019.
- [2] Y. J. He, B. C. Liu, B. Zhang, Z. B. Cheng, and Z. F. Qiu, "Overview on Satellite Remote-sensing Methods for Sea-surface-current Measurement," *Guangxi Sciences*, vol. 22, no. 3, pp. 294–300, 2015.

- [3] B. Chapron, F. Collard, F. Ardhuin, "Direct measurement of ocean surface velocity from space: Interpretation and validation," *J. Geophys. Res.: Oceans*. vol. 110, no. C7, pp. C07008, 2005.
- [4] M. J. Rouault, A. Mouche, F. Collard, J. A. Johannessen, B. Chapron, "Mapping the aguilas current from space: An assessment of ASAR surface current velocity," *J. Geophys. Res.: Oceans*. vol. 115, pp. C10026, 2010.
- [5] M. W. Hansen, F. Collard, K. F. Dagestad, J. A. Johannessen, B. Chapron, "Retrieval of sea surface range velocity from envisat ASAR Doppler centroid measurements," *IEEE Trans. Geosci. Remote Sens.* vol. 49, no. 10, pp. 3582–3592, 2011.
- [6] R. M. Goldstein, H. A. Zebker, "Interferometric radar measurement of ocean surface currents," *Nature*. vol. 328, pp. 707–709, 1987.
- [7] R. Romeiser, D. R. Thompson, "Numerical study on the along-track interferometric radar imaging mechanism of oceanic surface currents," *IEEE Trans. Geosci. Remote Sens.* vol. 38, no. 1, pp. 446–485, 2000.
- [8] R. Romeiser, H. Runge, "Theoretical evaluation of several possible along-track InSAR modes of TerraSAR-X for ocean current measurements. *IEEE Trans., Geosci. Remote Sens.* vol. 45, no. 1, pp. 21–35, 2007.
- [9] H. C. Graber, D. R. Thompson, R. E. Carande, "Ocean surface features and currents measured with synthetic aperture radar interferometry and HF radar," *J. Geophys. Res.: Oceans*. vol. 101, no. 11, pp. 25813–25832, 1996.
- [10] R. Romeiser, "Current measurements by Airborne Along-Track InSAR: Measuring Technique and Experimental Results," *IEEE J. Oceanic Eng.* vol. 30, no. 3, pp. 55–56, 2005.
- [11] J. V. Toporkov, D. Perkovic, G. Farquharson, M. A. Sletten, S. J. Frasier, "Sea surface velocity vector retrieval using dual-beam interferometry: First demonstration," *IEEE Trans. Geosci. Remote Sens.* vol. 43, no. 11, pp. 2494–2502, 2005.
- [12] R. Romeiser, H. Breit, M. Eineder, H. Runge, P. Flament, K. De Jong, J. Vogelzang, "Current Measurements by SAR Along-Track Interferometry From a Space Shuttle," *IEEE Trans. Geosci. Remote Sens.* vol. 43, no. 10, pp. 2315–2324, 2005.
- [13] R. Romeiser, H. Runge, S. Suchandt, J. Sprenger, H. Weilbeer, A. Sohrmann, D. Stammer, "Current Measurements in Rivers by Spaceborne Along-Track InSAR," *IEEE Trans. Geosci. Remote Sens.* vol. 45, no. 12, pp. 4019–4031, 2007.
- [14] R. Romeiser, S. Suchandt, H. Runge, U. Steinbrecher, S. Grunler, "First analysis of TerraSAR-X along-track InSAR-derived current field," *IEEE Trans. Geosci. Remote Sens.* vol. 48, no. 2, pp. 820–829, 2010.
- [15] S. Suchandt, H. Runge, "Ocean Surface Observations Using the TanDEM-X Satellite Formation," *IEEE J-Stars*. vol. 8, no. 11, pp. 5096–5105, 2017.
- [16] E. Makhoul, S. V. Baumgartner, M. Jager, A. Broquetas, "Multichannel SAR-GMTI in Maritime Scenarios With F-SAR and TerraSAR-X Sensors," *IEEE J-Stars*. vol. 8, no. 11, pp. 5052–5067, 2017.
- [17] F. Biondi, P. Addabbo, C. Clemente, D. Orlando, "Measurements of surface river Doppler velocities with along-track InSAR using a single antenna," *IEEE J-Stars*. vol. 13, pp. 987–997, 2020.
- [18] T. Yoshida, O. Kazuo, C. S. Yang, "Application of MA-ATI SAR for Estimating the Direction of Moving Water Surface Currents in Pi-SAR2 Images," *IEEE J-Stars*. vol. 14, pp. 2724–2730, 2021.
- [19] H. Runge, C. Laux, M. Gabele, R. Metzger, M. Gottwald, "Performance analysis of virtual multi-channel modes for TerraSAR-X," Proceedings of the 6th European Conference on Synthetic Aperture Radar (EUSAR 2006), Dresden, Germany, 2006.
- [20] S. Chiu, C. Livingstone, I. Sikaneta, C. Gierull, P. Beaulne, "Radarsat-2 moving object detection experiment(MODEX)," Proceedings of the IGARSS 2008 - 2008 IEEE International Geoscience and Remote Sensing Symposium, Boston, Massachusetts, USA, 2008.
- [21] H. Runge, S. Suchandt, R. Kahle, "Ocean current retrievals from TerraSAR-X and TanDEM-X data," TanDEM-X Science Team Meeting, Oberpfaffenhofen, Germany: DLR, 2013.
- [22] R. Romeiser, "The future of SAR-based oceanography: High-resolution current measurements by along-track interferometry," *Oceanography*. vol. 26, no. 2, pp. 93–99, 2013.
- [23] R. Romeiser, H. Runge, S. Suchandt, R. Kahle, C. Rossi, P. S. Bell, "Quality Assessment of Surface Current Fields From TerraSAR-X and TanDEM-X Along-Track Interferometry and Doppler Centroid Analysis," *IEEE Trans. Geosci. Remote Sens.* vol. 52, no. 5, pp. 2759–2772, 2013.
- [24] S. J. Frasier, A. J. Camps, "Dual-Beam Interferometry for Ocean Surface Current Vector Mapping," *IEEE Trans. Geosci. Remote Sens.* vol. 39, no. 2, pp. 401–414, 2001.
- [25] W. J. Wen, X. L. Qiu, "Research on Turning Motion Targets and Velocity Estimation in High Resolution Spaceborne SAR," *Sensors*. vol. 20, no. 8, pp. 2201, 2020.
- [26] Q. J. Zhang, "System Design and Key Technologies of the GF-3 Satellite," *Acta Geod Cartogr Sin.* vol. 46, no. 3, pp. 269–277, 2017.
- [27] S. Suchandt, H. Runge, H. Breit, U. Steinbrecher, A. Kotenkov, U. Balss, "Automatic extraction of traffic flows using TerraSAR-X along-track interferometry," *IEEE Trans. Geosci. Remote Sens.* vol. 48, no. 2, pp. 807–819, 2010.
- [28] B. Han, C. B. Ding, L. H. Zhong, J. Y. Liu, X. L. Qiu, Y. X. Hu, B. Lei, "The GF-3 SAR data processor," *Sensors*. vol. 18, no. 3, pp. 835, 2018.
- [29] L. M. Novak, S. D. Halversen, G. Owirka, M. Hiett, "Effects of polarization and resolution on SAR ATR," *IEEE Trans. Aerosp. Electron. Syst.* vol. 33, no. 1, pp. 102–115, 1997.
- [30] P. Wang, J. Chong, H. Wang, "Ship detection of the airborne SAR images," Proceedings of the IGARSS 2000 - IEEE 2000 International Geoscience and Remote Sensing Symposium, Honolulu, HI, USA, 2000.
- [31] R. Romeiser, M. Schwäbisch, J. Schulz-Stellenfleth, D. R. Thompson, R. Siegmund, A. Niedermeier, W. Alpers, S. Lehner, "Study on concepts for radar interferometry from satellites for ocean (and Land) applications (KoRIOLiS)," Univ.Hamburg, Hamburg, Germany. Final Report 50EE0100, 2002.



© 2020 by the authors. Submitted for possible open access publication under the terms and conditions of the Creative Commons Attribution (CC BY) license

(<http://creativecommons.org/licenses/by/4.0/>).